



Investigating the effect of Cu-rich phase on the corrosion behavior of Super 304H austenitic stainless steel by TEM



X.Y. San^{a,1}, B. Zhang^{a,*,1}, B. Wu^a, X.X. Wei^a, E.E. Oguzie^b, X.L. Ma^{a,c,*}

^a Shenyang National Laboratory for Materials Science (SYNL), Institute of Metal Research, Chinese Academy of Sciences, Wenhua Road 72, 110016 Shenyang, China

^b Electrochemistry and Materials Science Research Laboratory, Department of Chemistry, Federal University of Technology Owerri, PMB 1526 Owerri, Nigeria

^c School of Materials Science and Engineering, Lanzhou University of Technology, Langongping Road 287, 730050 Lanzhou, China

ARTICLE INFO

Keywords:

Super 304H stainless steel
Cu-rich phase
TEM
Corrosion

ABSTRACT

The precipitation of a fine Cu-rich phase dispersedly distributed in the austenitic matrix can impart the novel properties of Super 304H SS. However, the contributions have not been well understood due to the difficulty encountered in obtaining precise experimental information on the corrosion events introduced by the nano-sized Cu-rich precipitates. In this work, we have applied TEM and clarified the dissolution occurred in Cu-rich phase and the dissolution-induced evolution in structure and chemistry on the surface. This work enabled us glean atomic scale insights on the effect of the Cu-rich phase on the corrosion behavior of the Super 304H SS.

1. Introduction

Super 304H stainless steel (Super 304H SS), newly developed by the addition of alloying elements Cu, Nb and N on the basis of 18Cr-8Ni stainless steel [1–4], is being widely used in ultra-super critical fossil boilers because of its superior high temperature strength [5], oxidation resistance and steam corrosion resistance [6]. The mechanical properties of Super 304H SS have been extensively investigated [7–13]. However, the data available on the corrosion behavior is limited [14,15]. Indeed, investigating the role of the alloying elements on the improved corrosion resistance is key to clearer understanding of the corrosion behavior of the Super 304H SS [15]. The element Nb is a strong carbide and nitride former, which has been recognized to have the capacity to inhibit the formation of Cr-rich $M_{23}C_6$ carbides at grain boundaries and thus decrease the risk of IGC (intergranular corrosion) [16–18]. It is worth noting that the main features of Super 304H SS derive from the presence of the alloying element Cu, which induces precipitation of fine Cu-rich phases dispersedly distributed in the austenitic matrix [3]. Usually, the nanoscale Cu-rich precipitated phases have a cube-on-cube orientation relationship with the austenite matrix [19,20], which offer added precipitation hardening [3,21]. However, in terms of corrosion performance, the contribution of Cu to the superior corrosion resistant properties of Super 304H SS has not been well understood, due essentially to paucity of precise experimental information on modifications to the initial corrosion process, as induced by the

nano-sized Cu-rich precipitates.

The effects of copper-alloying in corrosion resistance of stainless steels have been presented in numerous publications [22–33]. Usually, the addition of copper to ferritic, austenitic or duplex steels improves the resistance to uniform corrosion in sulfuric acid [23–26], whereas shows positive [27–30] or negative effects to the local corrosion [31–33]. The effect of the alloying element copper has been implied to be ascribed to the alteration in the microstructure and its dissolution as well as re-deposition process. Actually, Cu has long been recognized as a mysterious alloying element. For example, Cu oversaturation in antibacterial stainless steels yields Cu in form of either a solid solution and/or a nanoscale Cu-rich phase, which have the key role in the antibacterial action [34]. The design is mainly based on the mechanism that elemental Cu in either form can slowly dissolve into the electrolyte from the stainless steel. Such preferential dissolution of Cu in form of Cu-rich phases is also a key feature of the initial corrosion stage.

For the traditional 304 austenitic stainless steel, great efforts have been put in towards understanding the effects of the non-metallic inclusions and precipitates on the corrosion behaviors for a long time [35,36]. By extension then, the novel properties of Super 304H SS must be partly ascribed to the Cu-rich phase, which indeed constitutes the main structural difference.

In the present work, we have applied TEM technique to identify the role of elemental Cu on the corrosion behavior of Super 304H SS, via tracking the evolution in structure and chemistry of the Cu-rich phase

* Corresponding authors at: Shenyang National Laboratory for Materials Science (SYNL), Institute of Metal Research, Chinese Academy of Sciences, Wenhua Road 72, 110016 Shenyang, China.

E-mail addresses: bozhang@imr.ac.cn (B. Zhang), xlma@imr.ac.cn (X.L. Ma).

¹ These authors contributed equally to this work.

as well as the solid-solution Cu at various stages of the corrosion process.

2. Experimental procedure

The Super 304H austenitic stainless steel (Super 304H SS) with nominal composition of Fe-0.1C-18Cr-9.3Ni-0.4Nb-0.2Si-0.8Mn-0.1N-3Cu was chosen in this study. The as-cast alloy were solution treated at 1200 °C for 2 h and then aged at 650 °C in air for 5000 h.

2.1. TEM specimen preparation

The steel was sliced into pieces with the thickness of 300 μm. The steel piece was ground using silicon carbide papers to 80 μm and then was die-cut in disks with diameter of 3 mm. The samples were ground using variant grit silicon carbide papers, polished with diamond paste to 20 μm finish, and finally thinned by ion-milling. After the first round of TEM observations, the specimens were plasma-cleaned and then immersed in the 3.5 wt% NaCl solution at room temperature for 30 min. The TEM specimens in the immersion tests were cleaned in distilled water, dried, plasma-cleaned and then transferred into the TEM for further investigation.

The cross-sectional TEM specimen was prepared by the conventional method. Two surfaces of two samples were bonded face-to-face and then thinned by grinding, dimpling and ion-milling.

2.2. HAADF-STEM imaging

A Tecnai G2 F30 TEM, equipped with a high-angle-angular-dark-field (HAADF) detector and X-ray dispersive spectrometer (EDS) systems, was used for recording the evolution process of the copper-rich phase precipitates. An aberration-corrected TEM (Titan³™ G2 60–300 microscope fitted with a high brightness field emission source, a monochromator, and a double Cs correctors from CEOS) was operated at 300 kV for high resolution TEM (HRTEM) and high resolution HAADF scanning transmission microscope (HR-HAADF-STEM) imaging. Before EDS and HR-STEM work, the TEM specimens were treated in a Fischione plasma cleaner for 8 min with a H₂/O₂ plasma recipe for removing the surface contamination.

2.3. Electrochemical experiments

A traditional three-electrode system was used in electrochemical experiments. The working electrode was the stainless steel specimen, a platinum foil was the counter electrode and a saturated calomel electrode (SCE) is the reference electrode. AUTOLAB PGSTAT302N electrochemical workstation was used in potentiodynamic polarization measurements, at a scan rate 0.33 mV/s. The tested solution of 3.5 wt% NaCl electrolytes was maintained at room temperature. Before electrochemical measurements, the Super 304H SS ingot was cut into 1 cm × 1 cm × 0.3 cm slices, which were then ground using various grit silicon carbide papers and polished with diamond paste to 20 μm finish, washed by distilled water, and degrease with acetone. The specimens were sealed with thread sealing tape and olefin resin.

3. Results and discussion

3.1. Microstructure of Super 304H SS

Fig. 1a–c is the HAADF-STEM image combined with EDS mapping analysis showing the type and distribution of the fine precipitates. A large number of precipitated particles are found at twin boundaries, large-angle grain boundaries and at the interior of the grains, wherein the precipitates at the twin boundaries feature a few tens of nanometers in size and they have a higher density compared with the interior of grains. In contrast, the precipitates at the large-angle grain boundaries

decreases remarkably in density and they have relatively larger size. EDS mapping analysis indicates that the fine precipitates can be classified into Cu- (major) and Nb-containing (minor) phases. Meanwhile, larger Cr-rich precipitates (Fig. 1c) are also found at grain boundary with a few hundreds of nanometers. Combined the high resolution HAADF-STEM imaging with the Fourier transform, the precipitates are identified to be fcc-structured Cu-rich phase and NbC (Fig. 1d), which have been reported in some previous work [20]. Due to aging at the sensitization temperature 650 °C, some relatively larger chromium-rich carbides (M₂₃C₆) with a few hundreds of nanometer scale are identified to precipitate at grain boundaries (Fig. 1e). Size distributions of the Cu-rich phase are obtained statistically from 120 particles located at twin-boundaries and at the interior of grains (seen in Fig. 2), most of which are in the range of 15–45 nm.

3.2. Corrosion behavior of Super 304H SS

The frequently-used electrochemical polarization measurements were firstly performed on the Super 304H SS in order to characterize the fundamental corrosion behavior. When the specimen was immersed in the 3.5 wt% NaCl electrolyte, the open circuit potential (OCP) was observed to shift dramatically to the positive direction with the amplitude of about 200 mV (Fig. 3), implying that some initial corrosion events occurred at this stage yielding a possibly enhanced corrosion resistance after immersion in the chloride-containing electrolyte. For further clarification, the potential dynamic polarization curves were recorded for the specimens immediately after immersion into the electrolyte and again after 1 h of immersion in the 3.5% NaCl electrolyte. Some typical potentiodynamic polarization curves are shown in Fig. 4a, it is seen that all the pre-immersed samples feature a noble shift of the OCP and a great decrease in the passive current density, which is indeed a unique and abnormal phenomenon since chloride usually decreases the stability of the passive film yielding the increase of the passive current density. The effect of long-term immersion on the pitting potential (E_{pit}) was also evaluated and the pitting potential data is generally scattered. Many samples were tested including free-immersed and pre-immersed samples (Fig. 4a). The distributions of E_{pit} values were plotted as illuminated in Fig. 4b. Cumulative probability shown in the vertical was calculated by a mean rank method: $P_{\text{cum}} = i/(N + 1)$, where P_{cum} is the cumulative probability of measured pitting potential (E_{pit}), i is the order in the total number N ($i = 1, 2, 3, \dots, N$). In Fig. 4b, it is indicated that the E_{pit} is not altered evidently by pre-immersion.

Some corrosion events are expected to occur, leading to an evolution in structure and surface state which eventually yields the observed alteration in corrosion behavior of the Super 304H SS. Without doubt, the nanometer dimensions of the dispersed Cu-rich phases means that experimental evidence must necessarily be acquired at the sub-nano scale, in order to clarify the expected evolution in structure and surface state, which determine the corrosion behavior of the Super 304H SS.

3.3. Evolution in structure and chemistry of the Cu-rich phase with corrosion

HAADF-STEM images and EDS mapping analysis of specimens before and after immersion in NaCl electrolyte are shown in Fig. 5. Fig. 5a is the HAADF-STEM image showing the distribution of Cu-rich phase particles in the austenitic matrix after long time aging. The Cu-rich phase is sphere and of nanometer dimensions. The incoherent HAADF-STEM images from high-angle scattered electrons yields strong atomic number (Z) contrast [37], in response to the local variability of chemical composition and/or thickness contribution of the different species. So the local dissolution should lead to a darker contrast in such a mode. After the first round of TEM observations, the specimens were re-immersed in the 3.5% NaCl media for 30 min, retrieved, cleaned and then subjected to another round of TEM observations.

The obtained images (shown in Fig. 5h) revealed that some original

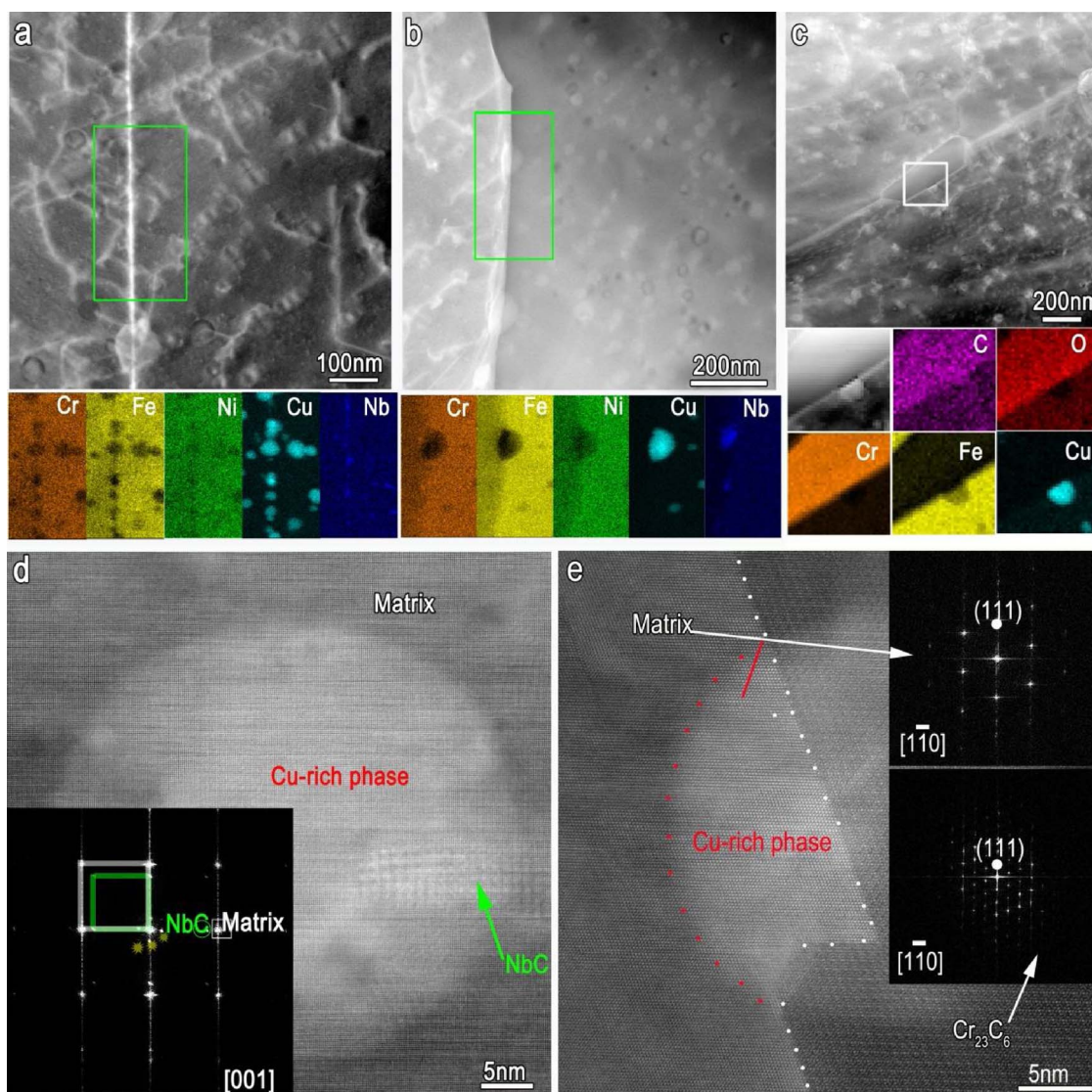


Fig. 1. Identification of the precipitates in the Super 304H SS. (a) HAADF-STEM images and EDS mapping analysis showing the distribution and composition of precipitates at a twin boundary. The elemental maps underneath the HAADF-STEM image are acquired in the rectangular area. (b–c) HAADF-STEM images and EDS mapping analysis showing the distribution and composition of precipitates at the large-angle grain boundaries. The elemental maps underneath each HAADF-STEM image correspond to the composition information in the marked area across the grain boundary. (d) High-resolution HAADF-STEM images viewed along $[001]_{\text{copper}}$ and $[001]_{\text{Matrix}}/[001]_{\text{NbC}}$ showing the coexistence of Cu-rich precipitate and NbC embedded in the matrix. The inset is FFT image showing the orientation relationships (OR). (e) High-resolution HAADF-STEM images viewed along $[1-10]_{\text{Cr}_{23}\text{C}_6}/[1-10]_{\text{copper}}$, $[1-10]_{\text{Matrix}}$ zone-axis. The inset is FFT image for phase identification. It is seen that the Cu-rich phase, NbC, Cr_{23}C_6 and matrix display the cube-on-cube crystallographic OR. The white dotted line shows the interface of Cr_{23}C_6 with matrix and Cu-rich phase, and the red dotted line outlines the interface of Cu-rich phase/matrix. (For interpretation of the references to colour in this figure legend, the reader is referred to the web version of this article.)

bright-contrast Cu-rich particles had become darker, implying that the Cu-rich phase had been dissolved. Meanwhile, some Cu-rich particles remain unattacked (labeled by white arrows). It is also seen that the small pits left by the dissolution of Cu-rich phase show varied degrees of darker contrast, lightly darker (labeled by green arrows) and deeply darker (labeled by blue arrows). EDS mapping analysis was performed on the settled zone within the white rectangle as marked in Fig. 5a and Fig. 5h (including two Cu-rich particles), focusing on the chemistry evolution before (Fig. 5c–g) and after (Fig. 5j–n) immersion. A comparison of Figs. 5g and 5n reveals that the two Cu-rich particles have undergo complete dissolution, yielding the almost homogeneous contrast of alloying copper in map of Cu. Interestingly, the imperceptible evolution of the other elements can be followed alongside the dissolution of Cu-rich phase. The two particles display different contrast, where particle 1 shows relative darker contrast and particle 2 brighter contrast (Fig. 5b). Correspondingly, particle 1 has darker Cu map and particle 2 has brighter Cu map (Fig. 5g). This indicates the varied

copper content ascribed to the heterogeneous compositions between particles or different depth contributions of the two particles, alternatively. For the particle 1, the contrasts of the Cr (Fig. 5k) and Fe (Fig. 5l) maps is evidently enhanced compared to the pristine maps (Fig. 5d and e), indicating that the relative contents of Cr and Fe increased with Cu-rich particle dissolution. For the particle 2, the contrast evolution of the Cr and Fe maps are very different from that of particle 1. The dark spots representing the maps of Cr (Fig. 5k) and Fe (Fig. 5l) are bordered by a ring with brighter contrast. Indeed, such character is more obvious in the Fe map. Similarly, Fig. 5j shows the dark spots on the O map to be also bordered, though only lightly in particle 1 and thickly in particle 2, which implies that the oxide products formed around the border with dissolution of the Cu-rich phase. The combined features of the maps of elements Fe, Cr and O, suggest that the oxide product is likely to be Fe-Cr-containing oxide. In order to clarify this, we superimposed the O map on the Cr (Fig. 5o–r) as well as Fe (Fig. 5s–v) maps, while varying the opacity, in order to obtain

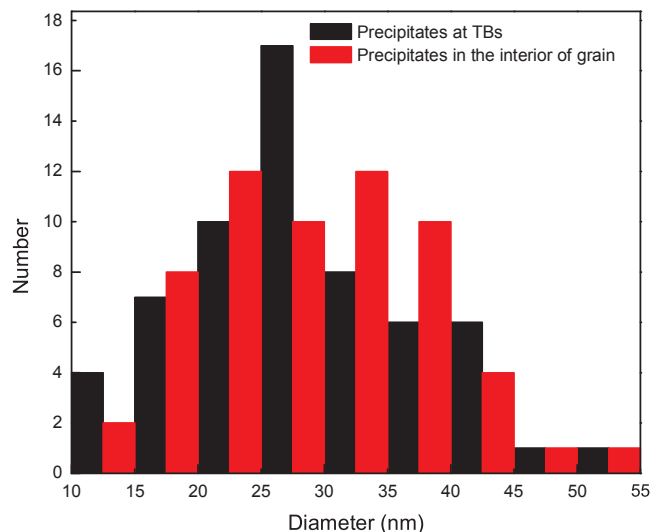


Fig. 2. Size distributions of the Cu-rich phase obtained statistically from 120 particles located at twin-boundaries (black column) and at the interior of grains (red column). (For interpretation of the references to colour in this figure legend, the reader is referred to the web version of this article.)

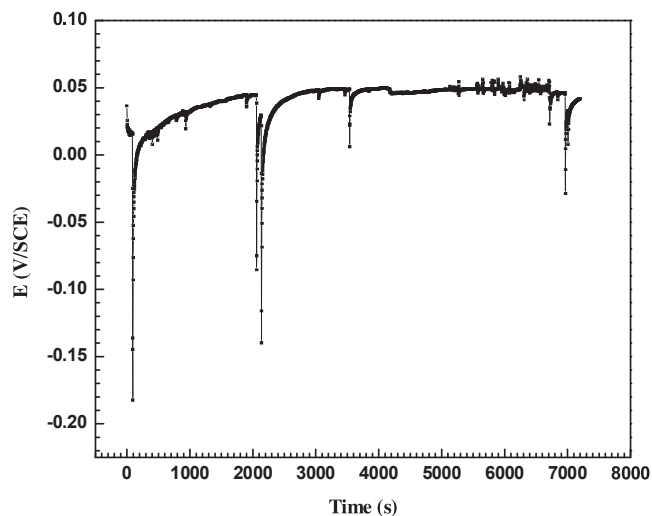


Fig. 3. OCP vs. time curve of 304 H SS in 3.5 wt% NaCl electrolyte.

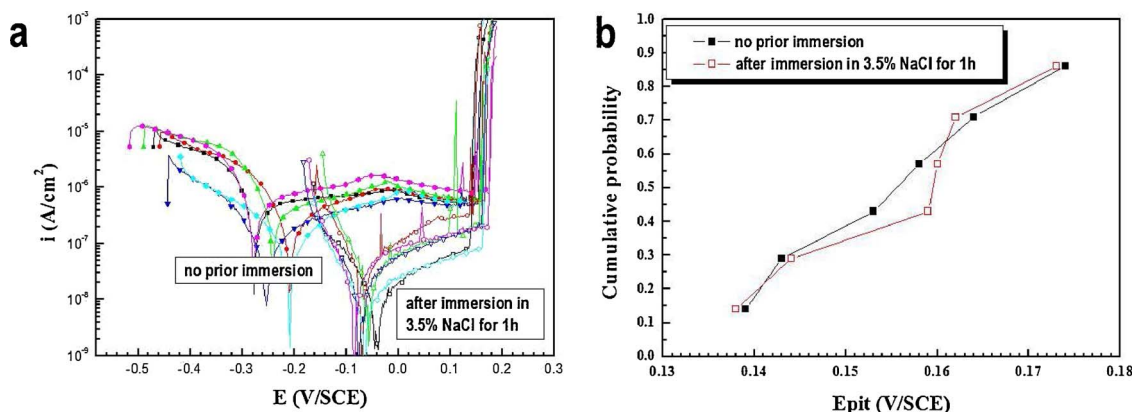


Fig. 4. The potentiodynamic polarization tests and pitting potential distributions of the samples before and after immersion. (a) Potentiodynamic polarization curves of Super 304 H SS were recorded on the specimens immediately after immersion into the 3.5 wt% NaCl electrolyte as well as after 1 h of immersion wherein 6 independent measurements were performed for each set. (b) The distribution of pitting potential of Super 304 H304H SS free of and with immersion.

composite graphs. The ring enriched in O exactly overlaps with the Cr and Fe rings confirming formation of Fe-Cr-containing oxide.

Usually, the varied degree of darker contrast of particles after corrosion (Fig. 5h) implies the Cu-rich particles underwent varied degrees of dissolution. Whereas, it is noteworthy that the Cu-rich particles are a few tens of nanometers, and the thickness of the thin zone (shown in Fig. 5 performed EDS mapping) was estimated to be about 50–100 nm through EELS technique, which yields that most of the Cu-rich particles might fail to penetrate the thin zone of the TEM specimen from top to bottom surface. Therefore, the morphology image in Fig. 5a representing the projections (like that illustrated in Fig. 6a) of the sphere Cu-rich phase would include four types of locations in the matrix, as shown in Fig. 6. If the particle is buried in the matrix as illustrated in Fig. 6b I, the particle would not be dissolved preferentially in the initial stage; if the particle is rooted in the matrix deeply (Fig. 6b II), the outer boarder zone (shadow filled) would be covered by the matrix yielding to an preferential dissolution at the center. Moreover, the beneath matrix is relatively thinner and thus contributes minor to the EDS signals; if the particle is embedded shallowly in the top surface (Fig. 6b III), the whole projection plane would totally be exposed to the surface and dissolved preferentially. The contribution of the beneath matrix to the EDS signals would be enhanced; if the particle penetrate the top and bottom surface of the thin zone of the TEM specimen (Fig. 6b IV), the matrix (major origins of elements Fe and Cr in EDS) would not contribute to the EDS signals yielding to a darker contrast of Fe and Cr and brighter contrast of Cu in the EDS maps. In another words, the varied contrast as well as evolution in contrast between particle 1 and 2 (Fig. 5), as aforementioned, can be ascribed to the different locations in the matrix, other than to the heterogeneous compositions between particles.

To further rationalize the above phenomena and interpretation, EDS line-scanning was performed on the other two adjacent Cu-rich particles (particle 3 and 4) within the red box as marked in Fig. 5a and h, which behave almost identical evolution with the particle 1 and 2. The EDS line-scanning spectroscopy is shown in Fig. 7. The major constituent of the stainless steel matrix is Fe, with Cr and Ni as alloying elements and trace amounts of Cu. As shown in Fig. 7a and c, compared with the matrix zone, the counts of element Cu dramatically increased and that of Fe, Cr and Ni decreased corresponding to Cu-rich phase particles. It has been reported that Cr, Fe, and Ni are slightly rejected from the Cu-enriched particle after long time aging [38]. Element O has a similar distribution trend going from the matrix to the Cu-rich phase, which means that the Cu-rich phase is not covered by an oxide film (passive film), rendering it more susceptible to preferential dissolution. At the Cu-rich phase/matrix interface, there exists a transition zone of a few nanometers, where the counts of elements Fe, Cr and Ni decreases and that of Cu increases gradually; until at the central zone, where the

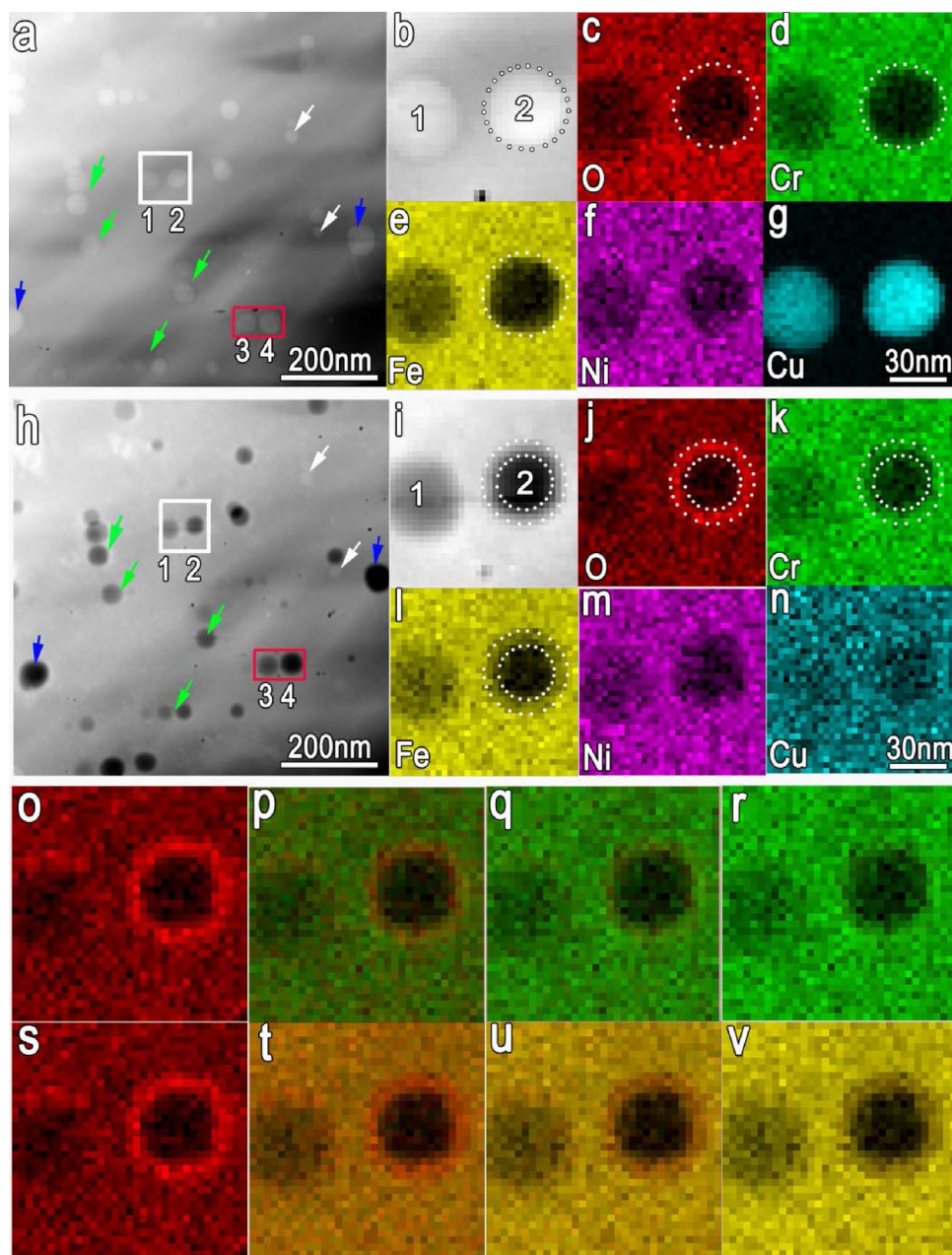


Fig. 5. Preferential dissolution of the Cu-rich phase induced evolution in local chemistry: (a) HAADF-STEM image showing nanometer Cu-rich phase particles with brighter contrast dispersedly distributed in the matrix. (b) Zoom-in image of the zone enclosed within the white box in (a), showing two Cu-rich particles. (c–g) EDS mapping analysis focusing on the two particles, (h) The same area as that in (a) after immersion in 3.5 wt% NaCl for 30 min. Preferential dissolution occurred in the Cu-rich phase particles, (i) The same two particles as that in (b) yield darker contrast after dissolution (j–n) EDS mapping analysis focusing on the evolution in chemistry of the two particles. (o–r) Composite graphs obtained by superimposing the O map (red) on the Cr map (green) with variant opacity of 10% (o), 30% (p), 50% (q) and 100% (r). (s–v) The composite image obtained by superimposing the O map (red) on the Fe map (yellow) with variant opacity of 10% (s), 30% (t), 50% (u) and 100% (v). The ring enriched in O just overlapped with the ring of Cr and Fe. (For interpretation of the references to colour in this figure legend, the reader is referred to the web version of this article.)

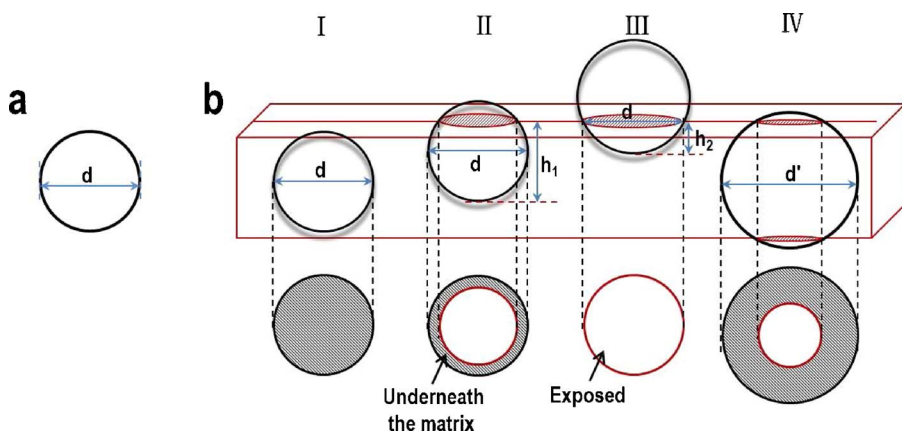


Fig. 6. Schematic maps illustrating the TEM sampling. (a) A particle with diameter of d . (b) Four types of locations of the Cu-rich particle in the matrix corresponding to the thin zone of a TEM specimen.

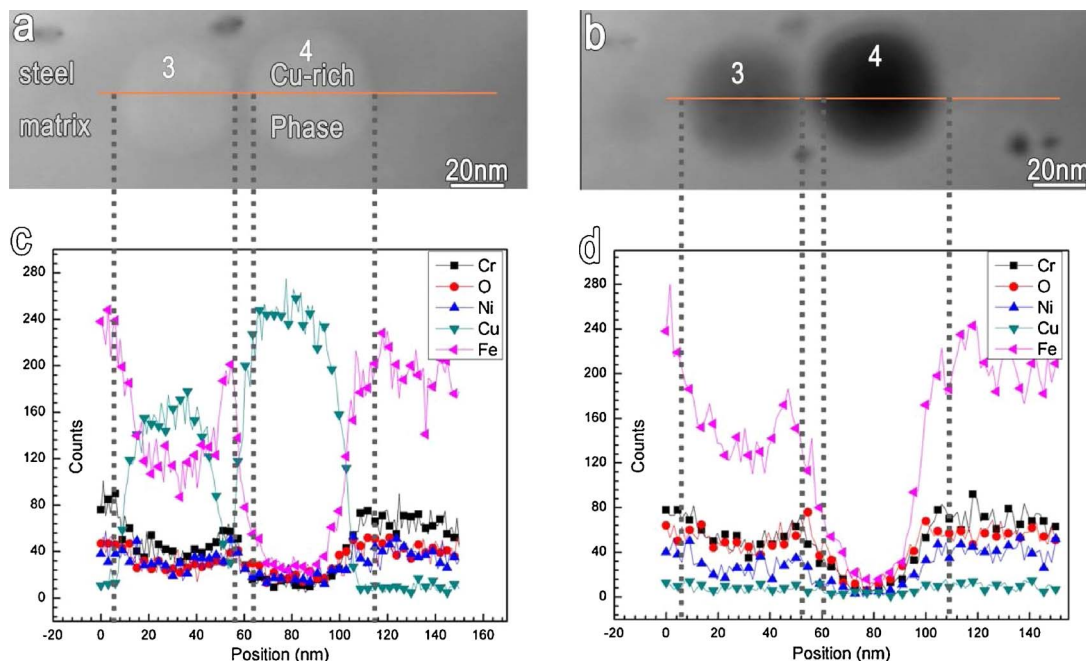


Fig. 7. EDS line-scanning analysis showing the composition distribution near and within the Cu-rich phase before and after corrosion. (a) HAADF-STEM images showing two adjacent Cu-rich particles (marked with the red rectangle in Fig. 4a and h). (b) The same particles as that in (a) after undergoing corrosion dissolution. EDS line-scanning analysis across the two particles before (c) and after (d) dissolution. (For interpretation of the references to colour in this figure legend, the reader is referred to the web version of this article.)

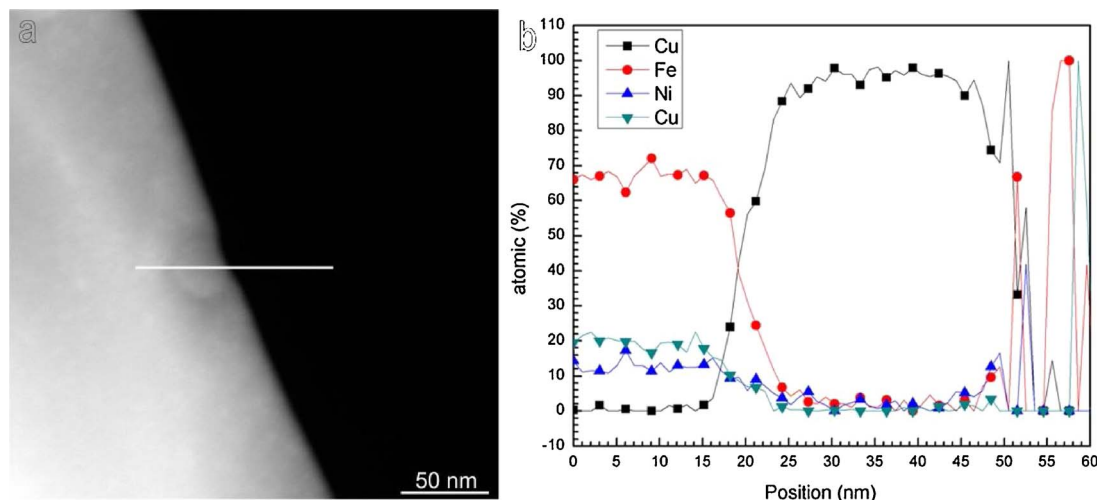


Fig. 8. (a) A HAADF-STEM image showing a Cu-rich particle located the outmost boundary site adjacent to the hole of the TEM specimen. (b) EDS line-scanning analysis across the particle along the white line in (a), wherein the specimen thickness is thin enough yielding the Cu-rich particle penetrate the top and bottom surface of the thin zone. In this case, the thickness at the central area of the Cu-rich particle should be identical.

Cu counts reaches the maximum value and correspondingly that of Fe, Cr and Ni is down to the minimum. The transition zone and the higher Cu counts at the center zone might result from the depth difference from the boarder to the center of the spherical cap (case as shown in Fig. 6b III). A particle located the outmost boundary site adjacent the hole of the TEM specimen was selected for the EDS line-scanning analysis, where the location of the Cu-rich particle corresponds to the illustration shown in Fig. 5b IV. In this case, the thickness at the central area of the Cu-rich particle should be identical. Correspondingly, we did observe the disappearance of the bulge in the copper-line (Fig. 8), which further confirmed that the thickness contribution on the EDS signals was nonnegligible and the copper content in single particle was almost homogeneous. A comparison of particle 3 and 4 reveals that particle 4 has relatively higher Cu counts and approximate zero counts of Fe, whereas particle 3 has relatively lower Cu counts and higher counts of Fe, as shown in Fig. 7c. After immersion, Cu counts dropped

dramatically to zero after corrosion (comparing Fig. 7c and 7d) indicating that the two Cu-rich particles have dissolved completely. The Fe counts increase after corrosion for particle 3 implying the pristine higher Fe counts are contributed by the beneath matrix. Namely, the particle 3 is embedded shallowly in the top surface (like that shown in Fig. 6b III) and the particle 4 penetrates the top and bottom surface (like that shown in Fig. 6b IV). The O counts increased after corrosion, which implies that the oxidation process occurred along with the dissolution. For the particle 3, the O counts increase evidently corresponding to the whole particle with more enhanced counts at the boundary site, in tandem with the EDS mapping results (Fig. 5j). Accordingly, it is postulated that the Cu-rich phase particle is not covered by a passive film, and is preferentially dissolved at the initial corrosion stage. With dissolution, the matrix beneath would be exposed and oxidized to form a layer of oxide film yielding to the increase of O counts in the EDS spectroscopy. For the particle 4, the O counts did not

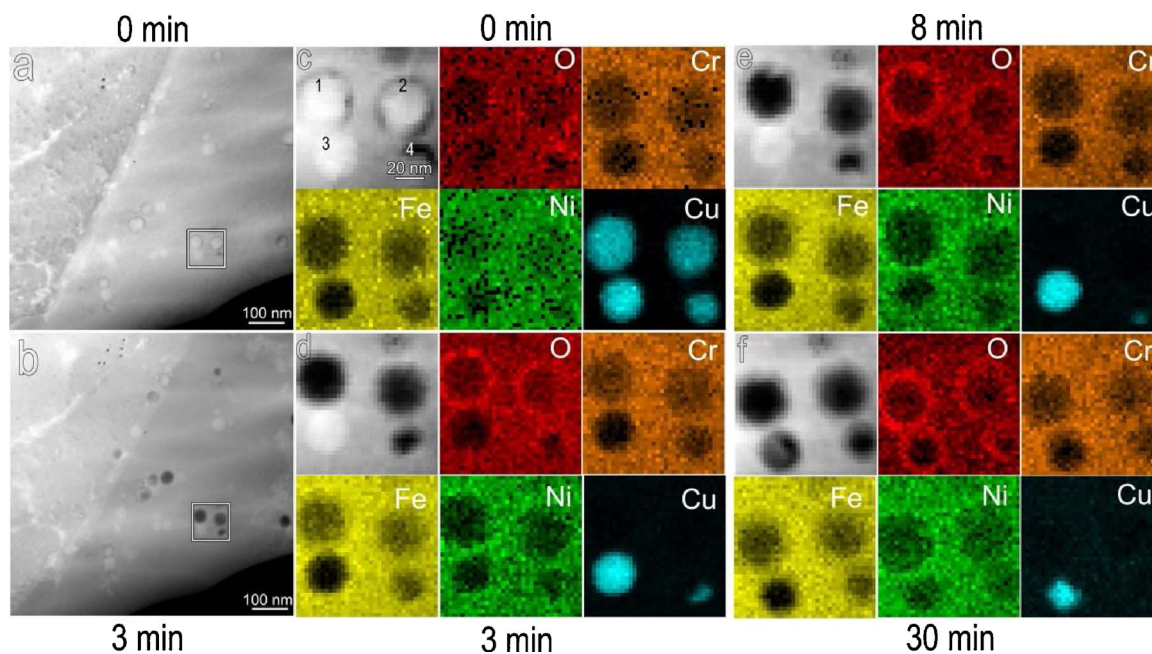


Fig. 9. Dissolution of the Cu-rich phase induced continuous evolution in local chemistry with varied immersion time: (a) HAADF-STEM image showing nanometer Cu-rich phase particles with brighter contrast dispersedly distributed in the matrix. (b) The same area as that in (a) after immersion in 3.5 wt% NaCl for 3 min. (c-f) Zoom-in image of the same zone enclosed within the white box in (a), showing four Cu-rich particles, and EDS maps with varied immersion times of 3 min, 8 min and 30 min.

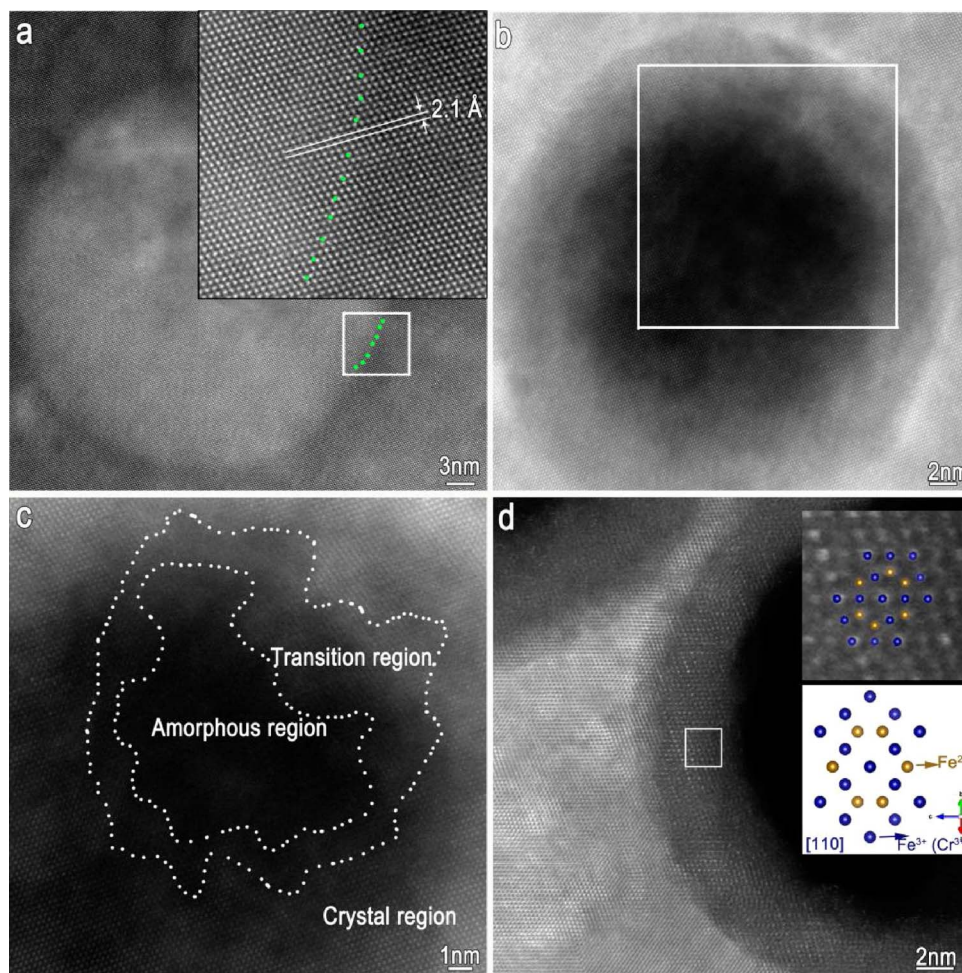


Fig. 10. Structural evolution with various degree of dissolution at the atomic scale: (a) High resolution HAADF-STEM image along the [110] direction showing the Cu-rich particle well orientated with the matrix. The inset is a zoom-in image of the zone enclosed within the white box in (a). The Cu-rich phase has a cube-on-cube crystallographic orientation with the Matrix. The (111) plane spacing of the Cu-rich phase and the matrix is approximately 2.1 Å. (b) High resolution HAADF-STEM image along the [110] direction showing the Cu-rich phase after slight dissolution. (c) Zoom-in image of the zone enclosed in square in (b) showing that the center zone had become amorphous due to dissolution, the immediate adjacent zone became the transition region wherein lattice fringes are still obvious. (d) High resolution HAADF-STEM image along the [110] direction showing the Cu-rich phase after severe dissolution. A spinel oxide ring was formed.

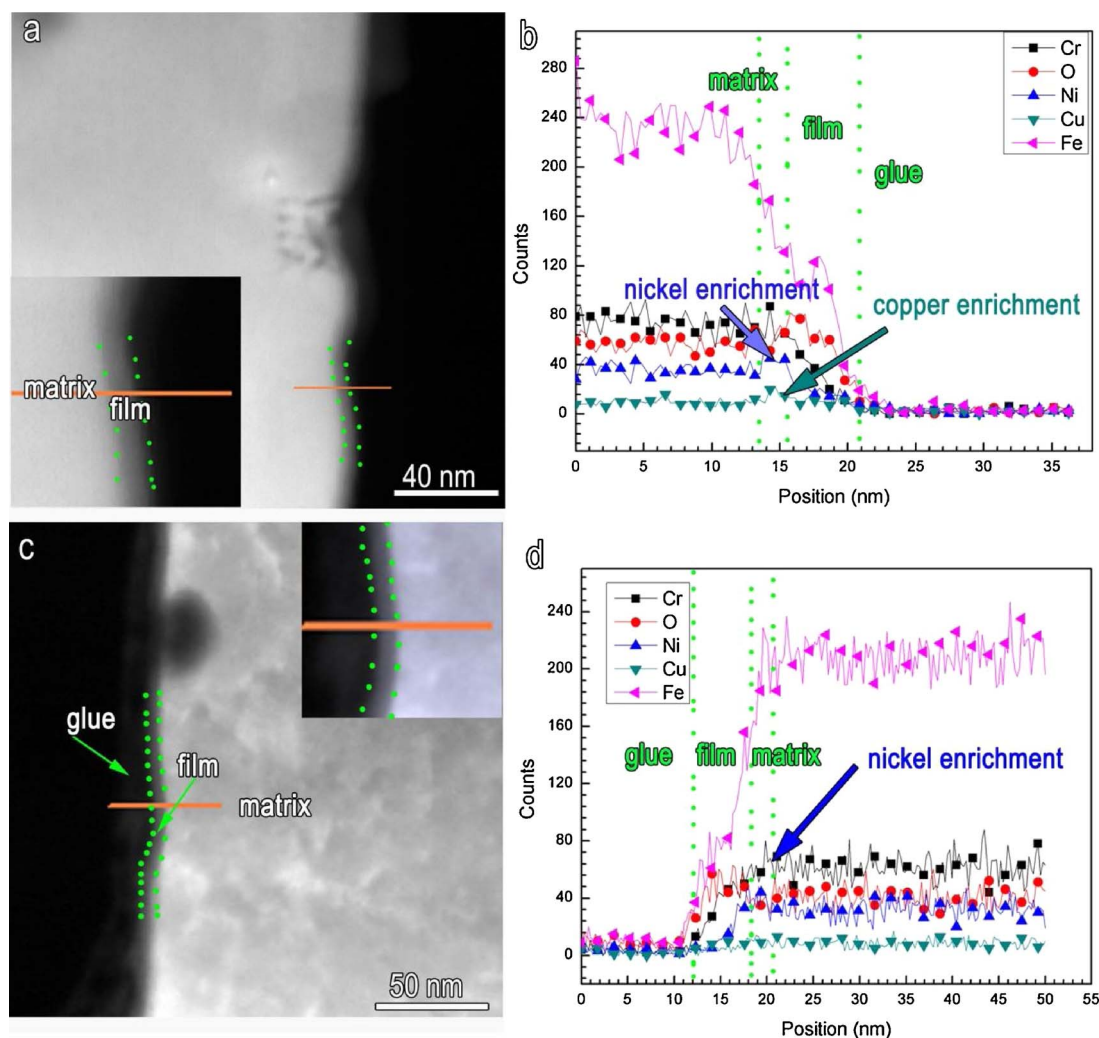


Fig. 11. HAADF-STEM imaging combined with EDS line-scanning analysis illustrating the evolution of the solid-solution state copper with corrosion: (a) HAADF-STEM image of the sectional specimen of the Super 304 H SS. The strip (marked by the green dish line, and enlarged and shown as the inset) with darker contrast is the air-formed oxide film with thickness of about 5 nm. (b) EDS line-scanning analysis along the orange line in (a). Ni and Cu enrichment is seen beneath the oxide film. (c) HAADF-STEM image of the sectional specimen of the Super 304 H SS after an immersion of 30 min in 3.5% NaCl electrolyte. (d) EDS line-scanning analysis along the orange line in (c). The Ni-enrichment below the oxide film remains identified, whereas the Cu-enrichment has disappeared after immersion. Insets in (a) and (c) are the zoom-in images of the area covering the zone marked by the green dish line. (For interpretation of the references to colour in this figure legend, the reader is referred to the web version of this article.)

increase as anticipated, except for the outermost dark ring, which is also in tandem with the EDS mapping results (Fig. 5j). This character is believed to result from the penetrated location type (like that shown in Fig. 6b IV) of the particle 4 yielding a hole at the center with the dissolution.

A series of HAADF-STEM images and EDS maps (Fig. 9) were obtained showing the evolution in structure and compositions of a given site (containing four Cu-rich particles) with varied immersion times of 3 min, 8 min and 30 min. From the Cu maps, particle 1 and 2 were dissolved completely, particle 3 was unattacked and particle 4 was dissolved partially after 3 min; further immersing to 8 min, particle 4 continued to be dissolved and particle 3 also was dissolved partially; to 30 min, particle 3 continued to be dissolved and particle 4 was exhausted. Correspondingly, a brighter ring got to appear on O map of particles 1 and 2 (completely dissolved) after 3 min immersion, whereas the ring around particle 4 (partially dissolved) was not evident and no ring appeared around particle 3 (undissolved); at 30 min, brighter rings around all the four particles became distinct, which indisputably implies that the oxidation process occurred along with the dissolution of the Cu-rich particles. From the series maps of Fe, it is seen that the contrast corresponding to particles 1 and 2 was enhanced at 3 min with the two particles dissolving completely; with further

immersion to 8 min and 30 min, the contrast of Fe corresponding to the sites of particles 1 and 2 did not become darker any longer, which implies that the “tiny pits” left by the dissolution of nano-scaled Cu-rich particles didn’t extend further into the steel matrix. The same phenomenon was also found even in the samples immersed for 24 h (not shown here). Evidently, unlike the well-known sulfide inclusion, the Cu-rich particles dissolve preferentially at the initial corrosion stage, but the dissolution would not play the fatal role to the corrosion resistance of the Super 304H SS.

A series of high resolution images were obtained at various stages of dissolution, which enable us track the structural evolution in the corrosion initiation and propagation process of the Cu-rich phase. Fig. 10a is the high resolution HAADF-STEM image along [110] zone axis, showing good orientation relationship between the Cu-rich phase and the matrix. After slight dissolution (partially dissolved), as shown in Fig. 10b–c, the Cu-rich particle started to show three regions: an amorphous region located at the center, a transition region immediately next to the center, wherein lattice fringes are still obvious, and a crystal region in the outer ring, which implies that the dissolution of the Cu-rich particle initiates at the center zone and then further propagates outwards. When the Cu-rich particle was dissolved completely as shown in Fig. 10d, interestingly, a well-defined novel crystal ring with darker

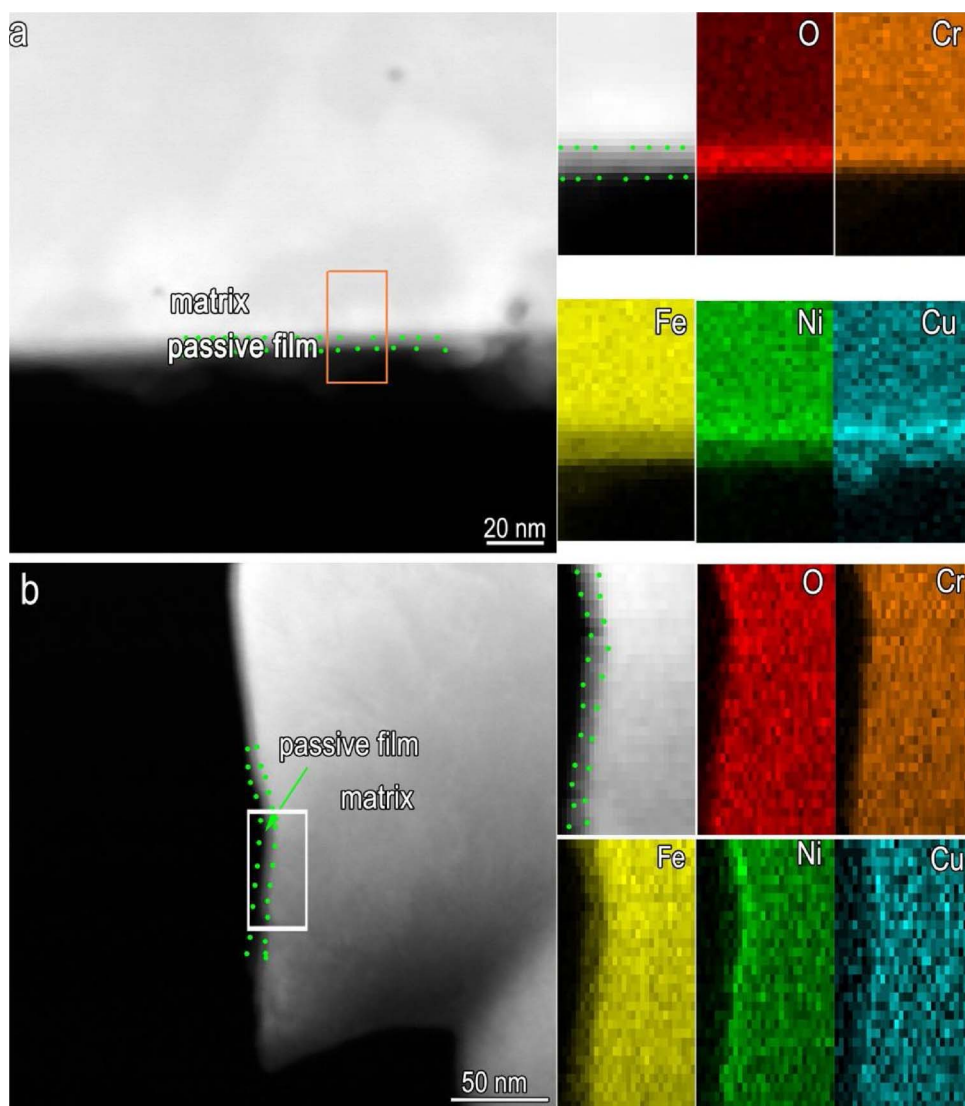


Fig. 12. HAADF-STEM imaging combined with EDS mapping analysis illustrating the evolution of the solid-solution state copper with corrosion: (a) HAADF-STEM image of the sectional specimen of the Super 304 H SS and EDS maps of the zone enclosed with the orange box. (b) HAADF-STEM image of the sectional specimen after an immersion of 30 min in 3.5% NaCl electrolyte, and the EDS maps correspond to the area enclosed with the white box. (For interpretation of the references to colour in this figure legend, the reader is referred to the web version of this article.)

contrast and width of about 5 nm was formed. This ring, which corresponds to the ring in particle 2 (Fig. 5i) and particle 4 (Fig. 7b), has spinel structure (Fig. 10d inserted) and was determined to be FeCr_2O_4 .

Evidently, the Cu-rich phase particle is not covered by a passive film and is preferentially dissolved at the initial corrosion stage. In other words, the passive film is disconnected by the dispersed Cu-rich particles at the nano-meter scale. With dissolution of Cu-rich phase, the beneath matrix would be oxidized to form amorphous oxide film and a spinel FeCr_2O_4 oxide ring is formed at the boundary, which is a passive film-like oxide in composition and structure. A spinel-like structure of the passive film on pure iron has been studied and confirmed by XRD [39], EXAFS [40–42] and STM techniques [43]. The extensive STM investigations indicated that the crystallinity of the passive film is highly dependent on the Cr content [44–47]. When the Cr content in the alloy was higher than 12%, the passive film would partially transit from well-defined spinel to partially amorphous. Mitrovic-Scepanovic et al. reported the existence of the spinel FeCr_2O_4 structure in the passive film on Fe-26Cr alloy [48]. As a result, the pristine disconnected passive film by the Cu-rich phase becomes more continuous when the Cu-rich phase particles are dissolved, which indisputably yields the improved stability of the passive film featured by the greatly noble shift in the OCP (Fig. 3), and the remarkable decrease in the passive current density (Fig. 4a).

3.4. Evolution of the solid-solution Cu with corrosion

In addition to the Cu-rich phase, another existing mode of alloying Cu is solid-solution state Cu in the matrix. Fig. 11 is the HAADF-STEM image and EDS line-scanning analysis of the sectional specimen, showing the distribution of the alloying element Cu before (Fig. 11a) and after immersion (Fig. 11c) in NaCl electrolyte. In Fig. 11a, the strip (marked by the green dish line) with darker contrast is the air-formed oxide film with thickness of about 5 nm. The EDS line-scanning analysis along the orange line was performed and the compositions are shown in Fig. 11b. It is seen that the Ni counts has a slight increase corresponding to the 1–2 nm depth immediately beneath the oxide film implying an enrichment of the element nickel. This was also extensively reported in the previous work [49–52]. Analogously, Cu enrichment below the oxide film is also indicated by the small peak in the Cu-K line. The EDS line-scanning spectroscopy obtained after an immersion of 30 min in NaCl electrolyte reveals that the Ni-enrichment below the oxide film remains unchanged, whereas the Cu-enrichment disappears, as shown in Fig. 11d. The same results are also confirmed by the EDS mapping analysis, as shown in Fig. 12. This implies that the solid-solution state Cu is enriched in the matrix immediately beneath the oxide film and is dissolved through the film when contacting the electrolyte.

4. Conclusion

With the application of HAADF-STEM imaging combined with EDS analysis, we have clarified the effect of the Cu-rich phase and solid-solution state copper on the corrosion behavior of the Super 304H SS through monitoring the structural and compositional evolutions with the corrosion process. The Cu-rich phase particle is preferentially dissolved at the initial corrosion stage. The “tiny pits” left by the dissolution of nano-scaled Cu-rich particles are oxidized and bordered by a newly formed spinel FeCr_2O_4 oxide ring, yielding the dissolution not to extend further into the steel matrix. The solid-solution state copper is enriched in the matrix immediately beneath the oxide film and is dissolved through the film when contacting the electrolyte.

Acknowledgements

This work is supported by the National Natural Science Foundation of China (No. 51771212, 11327901, 51390473), the Key Research Program of Frontier Sciences CAS (QYZDJ-SSW-JSC010), the Innovation Fund in IMR (2017-ZD05) and in SYNL (2017FP17). E.E.O. is grateful to the Chinese Academy of Sciences (CAS) for award of the CAS President's Fellowship.

References

- [1] Y. Sawaragi, S. Hirano, The development of a new 18-8 austenitic stainless-steel (0.1C-18Cr-9Ni-3Cu-Nb, N) with high elevated-temperature strength for fossil power boilers, *Mechan. Behav. Mater.-Vi* 1–4 (1992) D589–D594.
- [2] F. Masuyama, History of power plants and progress in heat resistant steels, *ISIJ Int.* 41 (2001) 612–625.
- [3] S. Tan, Z. Wang, S. Cheng, Z. Liu, J. Han, W. Fu, Effect of Cu content on aging precipitation behaviors of Cu-rich phase in Fe-Cr-Ni alloy, *J. Iron Steel Res. Int.* 17 (2010) 63–68.
- [4] J. Yuan, X. Wu, W. Wang, S. Zhu, F. Wang, The effect of surface finish on the scaling behavior of stainless steel in steam and supercritical water, *Oxid. Met.* 79 (2013) 541–551.
- [5] V.K. Gouda, M.M. Nassrallah, S.M. Sayed, N.H. Gerges, Failure of boiler tubes in power-plants, *Br. Corros. J.* 16 (1981) 25–31.
- [6] R. Wang, Z. Zheng, Q. Zhou, Y. Gao, Effect of surface nanocrystallization on the sensitization and desensitization behavior of Super304H stainless steel, *Corros. Sci.* 111 (2016) 728–741.
- [7] G. Bai, S. Lu, D. Li, Y. Li, Intergranular corrosion behavior associated with delta-ferrite transformation of Ti-modified Super304H austenitic stainless steel, *Corros. Sci.* 90 (2015) 347–358.
- [8] K.K. Alaneme, S.M. Hong, I. Sen, E. Fleury, U. Ramamurty, Effect of copper addition on the fracture and fatigue crack growth behavior of solution heat-treated SUS 304H austenitic steel, *Mater. Sci. Eng. A* 527 (2010) 4600–4604.
- [9] Y.F. Shen, N. Jia, Y.D. Wang, X. Sun, L. Zuo, D. Raabe, Suppression of twinning and phase transformation in an ultrafine grained 2 GPa strong metastable austenitic steel: experiment and simulation, *Acta Mater.* 97 (2015) 305–315.
- [10] A. Chen, J. Liu, H. Wang, J. Lu, Y.M. Wang, Gradient twinned 304 stainless steels for high strength and high ductility, *Mater. Sci. Eng. A* 667 (2016) 179–188.
- [11] A. Zielinski, G. Golanski, M. Sroka, J. Dobrzanski, Estimation of long-term creep strength in austenitic power plant steels, *Mater. Sci. Technol.* 32 (2016) 780–785.
- [12] S. Hermanova, L. Kander, J. Horvath, The effect of cold bending process and degradation at boiler conditions on the properties of new austenitic creep resistant steel Super 304H for boiler super-heaters tubes, *Mater. Sci. Forum.* 891 (2017) 230–234.
- [13] J. Horvath, J. Janovec, M. Junek, The changes in mechanical properties of austenitic creep resistant steels SUPER 304H and HR3C caused by medium-term isothermal ageing, *Solid State Phenom.* 258 (2017) 639–642.
- [14] Y.J. Ren, Y.Q. Chen, J. Chen, W. Li, C.L. Zhang, Electrochemical impedance studies for intergranular corrosion of Super 304H stainless steel, *Mater. Perform.* 55 (2016) 60–63.
- [15] G. Bai, S. Lu, D. Li, Y. Li, Effects of boron on microstructure and metastable pitting corrosion behavior of Super304H austenitic stainless steel, *J. Electrochem. Soc.* 162 (2015) C473–C481.
- [16] K. Ogawa, Y. Sawaragi, N. Otsuka, H. Hirata, A. Natori, S. Matsumoto, Mechanical and corrosion properties of high-strength 18-percent Cr austenitic stainless-steel weldment for boiler, *ISIJ Int.* 35 (1995) 1258–1264.
- [17] G. Bai, S. Lu, D. Li, Y. Li, Influences of niobium and solution treatment temperature on pitting corrosion behaviour of stabilised austenitic stainless steels, *Corros. Sci.* 108 (2016) 111–124.
- [18] J. Erneman, M. Schwind, P. Liu, J.O. Nilsson, H.O. Andren, J. Agren, Precipitation reactions caused by nitrogen uptake during service at high temperatures of a niobium stabilised austenitic steel, *Acta Mater.* 52 (2004) 4337–4350.
- [19] C. Chi, H. Yu, J. Dong, W. Liu, S. Cheng, Z. Liu, X. Xie, The precipitation strengthening behavior of Cu-rich phase in Nb contained advanced Fe-Cr-Ni type austenitic heat resistant steel for USC power plant application, *Prog. Nat. Sci.-Mater. Int.* 22 (2012) 175–185.
- [20] J.W. Bai, P.P. Liu, Y.M. Zhu, X.M. Li, C.Y. Chi, H.Y. Yu, X.S. Xie, Q. Zhan, Coherent precipitation of copper in Super304H austenite steel, *Mater. Sci. Eng. A* 584 (2013) 57–62.
- [21] X.M. Li, Y. Zou, Z.W. Zhang, Z.D. Zou, B.S. Du, Intergranular corrosion of weld metal of Super type 304H steel during 650 degrees c aging, *Corrosion* 68 (2012) 379–387.
- [22] N. Fuetes, R. Pettersson, Review-passive film properties and electrochemical response of different phases in a Cu-alloyed stainless steel after long term heat treatment, *J. Electrochem. Soc.* 163 (2016) C377–C385.
- [23] M. Seo, G. Hultquist, C. Leygraf, N. Sato, The influence of minor alloying elements (Nb, Ti and Cu) on the corrosion resistivity of ferritic stainless-steel in sulfuric-acid-solution, *Corros. Sci.* 26 (1986) 949–960.
- [24] G. Hultquist, M. Seo, T. Leitner, C. Leygraf, N. Sato, The dissolution behavior of iron chromium, molybdenum and copper from pure metals and from ferritic stainless-steels, *Corros. Sci.* 27 (1987) 937–946.
- [25] J.N. Yuan, L.C. Wen, W.H. Shen, The effect of copper on the anodic-dissolution behavior of austenitic stainless-steel in acidic chloride solution, *Corros. Sci.* 33 (1992) 851–859.
- [26] J.S. Lee, S.T. Kim, I.S. Lee, G.T. Kim, J.S. Kim, Y.S. Park, Effect of copper addition on the active corrosion behavior of hyper duplex stainless steels in sulfuric acid, *Mater. Trans.* 53 (2012) 1048–1055.
- [27] A.A. Hermas, K. Ogura, T. Adachi, Accumulation of copper layer on a surface in the anodic polarization of stainless-steel containing Cu at different temperatures, *Electrochim. Acta* 40 (1995) 837–844.
- [28] A.A. Hermas, K. Ogura, S. Takagi, T. Adachi, Effects of alloying additions on corrosion and passivation behaviors of type-304 stainless-steel, *Corrosion* 51 (1995) 3–10.
- [29] T. Ujiro, S. Satoh, R.W. Staehle, W.H. Smyrl, Effect of alloying Cu on the corrosion resistance of stainless steels in chloride media, *Corros. Sci.* 43 (2001) 2185–2200.
- [30] A. Pardo, M.C. Merino, M. Carboneras, F. Viejo, R. Arrabal, J. Munoz, Influence of Cu and Sn content in the corrosion of AISI 304 and 316 stainless steels in H_2SO_4 , *Corros. Sci.* 48 (2006) 1075–1092.
- [31] J. Banas, A. Mazurkiewicz, The effect of copper on passivity and corrosion behaviour of ferritic and ferritic-austenitic stainless steels, *Mater. Sci. Eng. A* 277 (2000) 183–191.
- [32] T. Sourisseau, E. Chauveau, B. Baroux, Mechanism of copper action on pitting phenomena observed on stainless steels in chloride media, *Corros. Sci.* 47 (2005) 1097–1117.
- [33] S.H. Jeon, S.T. Kim, I.S. Lee, J.H. Park, K.T. Kim, J.S. Kim, Y.S. Park, Effects of copper addition on the formation of inclusions and the resistance to pitting corrosion of high performance duplex stainless steels, *Corros. Sci.* 53 (2011) 1408–1416.
- [34] L. Ren, L. Nan, K. Yang, Study of copper precipitation behavior in a Cu-bearing austenitic antibacterial stainless steel, *Mater. Des.* 32 (2011) 2374–2379.
- [35] J. Stewart, D.E. Williams, The initiation of pitting corrosion on austenitic stainless-steel – on the role and importance of sulfide inclusions, *Corros. Sci.* 33 (1992) 457–463.
- [36] R.R. Ke, R. Alkire, Initiation of corrosion pits at inclusions on 304 stainless steel, *J. Electrochem. Soc.* 142 (1995) 4056–4062.
- [37] S.J. Pennycook, Structure determination through Z-contrast microscopy, in: Peter W. Hawkes PGMGC, V.-A. Marco (Eds.), *Advances in Imaging and Electron Physics*, vol. 123, Elsevier, 2002, pp. 173–206.
- [38] M. Murayama, Y. Katayama, K. Hono, Microstructural evolution in a 17-4 pH stainless steel after aging at 400 degrees C, *Metall. Mater. Trans. A* 30 (1999) 345–353.
- [39] U.R. Evans, The passivity of metals Part I: the isolation of the protective film, *J. Chem. Soc.* (1927) 1020–1040.
- [40] G.G. Long, J. Kruger, D.R. Black, M. Kuriyama, EXAFS study of the passive film on iron, *J. Electrochem. Soc.* 130 (1983) 240–242.
- [41] J. Robinson, F.C. Walsh, In-situ synchrotron-radiation X-ray techniques for studies of corrosion and protection, *Corros. Sci.* 35 (1993) 791–800.
- [42] M. Kerker, J. Robinson, A.J. Forty, In situ structural studies of the passive film on iron and iron chromium-alloys using X-ray absorption-spectroscopy, *Faraday Discuss.* 89 (1990) 31–40.
- [43] M.P. Ryan, R.C. Newman, G.E. Thompson, An STM study of the passive film formed on iron in borate buffer solution, *J. Electrochem. Soc.* 142 (1995) L177–L179.
- [44] V. Maurice, W.P. Yang, P. Marcus, XPS and STM investigation of the passive film formed on Cr(110) single-crystal surfaces, *J. Electrochem. Soc.* 141 (1994) 3016–3027.
- [45] M.P. Ryan, R.C. Newman, G.E. Thompson, A scanning-tunneling-microscopy study of structure and structural relaxation in passive oxide-films on Fe-Cr alloys, *Philos. Mag. B* 70 (1994) 241–251.
- [46] M.P. Ryan, R.C. Newman, G.E. Thompson, Atomically resolved stm of oxide film structures on Fe-Cr alloys during passivation in sulfuric-acid-solution, *J. Electrochem. Soc.* 141 (1994) L164–L165.
- [47] V. Maurice, W.P. Yang, P. Marcus, XPS and STM sTM study of passive films formed on Fe-22Cr(110) single-crystal surfaces, *J. Electrochem. Soc.* 143 (1996) 1182–1200.
- [48] V. Mitrovicsepanovic, B. Macdougall, M.J. Graham, Nature of passive films on Fe-26Cr alloy, *Corros. Sci.* 24 (1984) 479–490.
- [49] J.E. Castle, J.H. Qiu, The application of ICP-MS and XPS to studies of ion selectivity during passivation of stainless-steels, *J. Electrochem. Soc.* 137 (1990) 2031–2038.
- [50] V. Maurice, W.P. Yang, P. Marcus, X-ray photoelectron spectroscopy and scanning tunneling microscopy study of passive films formed on (100) Fe-18Cr-13Ni single-crystal surfaces, *J. Electrochem. Soc.* 145 (1998) 909–920.
- [51] E. Hamada, K. Yamada, M. Nagoshi, N. Makiishi, K. Sato, T. Ishii, K. Fukuda, S. Ishikawa, T. Ujiro, Direct imaging of native passive film on stainless steel by aberration corrected STEM, *Corros. Sci.* 52 (2010) 3851–3854.
- [52] K. Oh, S. Ahn, K. Eom, K. Jung, H. Kwon, Observation of passive films on Fe-20Cr-xNi (x = 0, 10, 20 wt.%) alloys using TEM and Cs-corrected STEM-EELS, *Corros. Sci.* 79 (2014) 34–40.